TURN UNCERTAINTY INTO PEACE OF MIND

Get ready for Beam Commissioning 4.0

Be the first to know about the all-new solution that revolutionizes your Beam Commissioning.
Quality. Performance. Peace of Mind.

Soon to be revealed.

**PROTECT +
ENHANCE +
SAVE LIVES**

System for image-guided resection of nonpalpable breast lesions: Proof of concept

Bruno Arsenali, Hugo W. A. M. de Jong, Max A. Viergever, and Kenneth G. A. Gilhuijs[a]

Image Sciences Institute, University Medical Center Utrecht, Heidelberglaan 100, 3584 CX Utrecht, The Netherlands

Purpose: In breast-conserving surgery (BCS), the cancer is sometimes incompletely excised, leading to reduced patient survival. To pursue complete excisions, radioactive seed localization (RSL) may be used to insert an iodine-125 seed into the tumor. The seed is used as a marker for the location of the tumor during surgery. RSL does not, however, show the extent of the tumor. Based on RSL, we pursue to visualize the seed location together with the extent from diagnostic images.

Methods: A system with two gamma-camera heads and two parallel-hole collimators was recently proposed to triangulate the location of an iodine-125 seed during BCS. In the present study, this system was extended with a range camera to visualize a sphere centered on the seed in relation to the breast. This sphere contains the entire tumor and thus defines the target volume for BCS. Physical experiments with acrylic block phantoms (thickness ranging from 3.5 to 6.5 cm) were performed to assess the absolute bias and the precision with which this sphere can be visualized.

Results: When a 6.5 cm thick phantom was used, along the horizontal plane, the target volume was visualized with an absolute bias and a precision of 2.1 and 0.8 mm, respectively. Along the vertical axis (i.e., z-axis), these values were 4.2 and 2.8 mm, respectively.

Conclusions: The proposed system visualizes the target volume with an absolute bias that may be acceptable for BCS. © *2018 American Association of Physicists in Medicine* [https://doi.org/10.1002/mp.12884]

Key words: breast-conserving surgery, gamma-camera system, intraoperative guidance, radioactive seed localization, range-camera system

1. INTRODUCTION

Breast-conserving therapy is the treatment of choice for most patients with early-stage breast cancer.[1] Based on evidence of the last 20 yr,[2,3] it is accepted that patients treated with radical mastectomy and those treated with breast-conserving surgery (BCS) and adjuvant therapy such as radiotherapy and chemotherapy have comparable survival rates. The percentage of incomplete excisions needs to be decreased to increase the survival of patients with early-stage breast cancer, as shown for example by Park et al.[4] and Singletary et al.[5]

Methods such as wire-guided localization and radio-guided occult lesion localization provide guidance for the excision of nonpalpable breast lesions, for example.[6,7] These methods provide intraoperative information about the location of the tumor, but limited or no information about the extent. The percentage of incomplete excisions may be further reduced by visualizing tumor location together with tumor extent during BCS. Such tumor extent may, for instance, be derived from preoperative images. Methods to achieve this prior to the first incision were previously described by Sakakibara et al.[8] and Nakamura et al.[9] A limitation of these methods is that they do not take tissue shifts into account after the first incision.

A method was recently reported to track the location of a radioactive seed (RS) together with a computer-generated bounding sphere around the tumor that is superimposed on the video images during the entire BCS.[10] This method consists of four steps. First, one iodine-125 seed is inserted in the tumor under mammographic or ultrasonic guidance. Second, the tumor is visualized in relation to the location of the RS in preoperative images of the breast. Third, a sphere that contains the entire tumor is centered on the RS in the same preoperative images. Fourth, this sphere is recentered on the intraoperative location of the RS (i.e., the location of the sphere is established within the operating room). This sphere thus defines the target volume for excision. Deviations in localization of the seed of 5 mm or less are acceptable to pursue negative surgical margins during BCS.[10]

Although the tracking mechanism of this system was recently described, there are no methods, to the best of our knowledge, to visualize a spherical target volume that is centered on the RS. Therefore, the aim of this study was to develop and evaluate such a method. With this in mind, a new system that has two gamma cameras and one range camera is investigated.

2. MATERIALS AND METHODS

Section 2.A describes the INCISE system (intraoperative navigation for breast cancer using presurgery

imaging). It introduces a new method to register data from two gamma-camera heads and one range camera. Section 2.B describes physical experiments that were conducted to assess the absolute bias and the precision with which the target volume centered on the RS can be visualized.

2.A. Overview of the system

The INCISE system was designed to integrate seamlessly into the current workflow of radioactive seed localization (RSL). Prior to surgery, as illustrated in the left part of Fig. 1, conventional breast imaging is repeated after RSL to visualize the seed in relation to the boundaries of the tumor. In these images, a sphere is manually centered on the RS and a radius of the sphere that encompasses the entire tumor with a safety margin of surrounding healthy tissue is established. The INCISE system, as illustrated in the right part of Fig. 1, is meant to be used during surgery. This system (Fig. 2) consists of a gamma-camera system (GCS; Section 2.A.1) and a range-camera system (RCS; Section 2.A.3). The GCS triangulates the location of the RS relative to the operating room at a speed of at least one frame per five seconds (Section 2.A.2). The RCS produces a video (i.e., a sequence of gray-level images) of the entire breast with a speed of approximately 30 frames per second. In addition, infrared imaging is used by the RCS to produce a cloud of surface points for each video image. This point cloud is mapped into the coordinate system of the GCS. For this purpose, a registration procedure with a calibration phantom is used (Section 2.A.4). Once the target volume and the point cloud are expressed in the same coordinate system, the distance between the surface of the target volume and the surface of the breast is estimated and visualized (Section 2.A.5).

2.A.1. The gamma-camera system (GCS)

The GCS is used during surgery to monitor the location of the RS. This system only records projection images of the RS. These images alone cannot be used to determine the location of the RS with respect to the breast surface. The RCS (Section 2.A.3) is invoked for this purpose.

The GCS has two gamma-camera heads (Philips Forte) and two low-energy, high-resolution (LEHR) collimators (ADAC Laboratories). Each gamma-camera head has one 52 cm wide, 64 cm long, and 9.5 cm thick thallium-doped sodium iodide crystal that is coupled to a total of 49 photomultiplier tubes. Each collimator has a hole length of 32.8 mm, hole size of 1.4 mm, and septal thickness of 0.152 mm. Two projection images were simultaneously obtained per acquisition. Each image had a pixel size of 4.7×4.7 mm. We used an energy window from 25 to 35 keV to suppress undesired counts. The method to establish the location of the RS is described in Section 2.A.2. The coordinates of this location along the x-axis, y-axis, and z-axis of the GCS are denoted by x_G, y_G, and z_G, respectively.
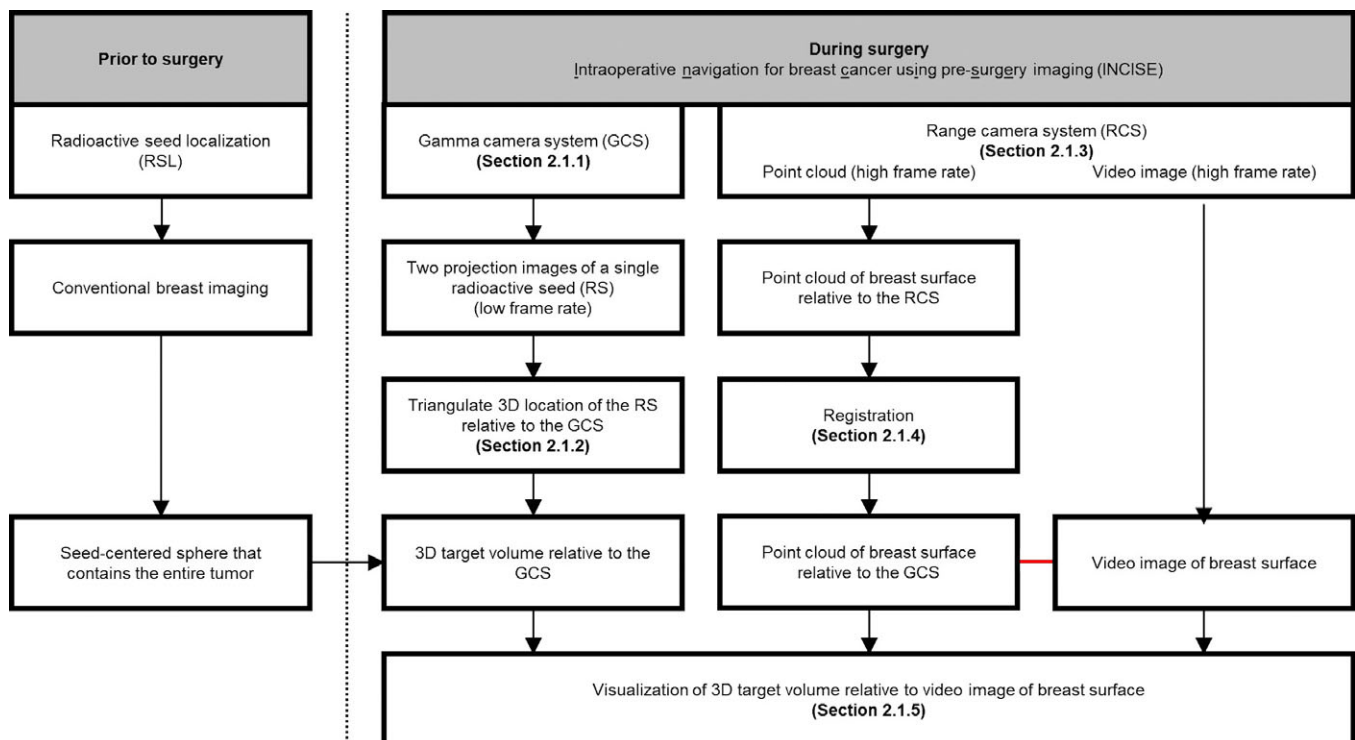

FIG. 1. Flowchart outlining the structure of Materials and Methods. The horizontal red line indicates one to one point-to-pixel correspondence between the points of the point cloud and the pixels of the video image. [Color figure can be viewed at wileyonlinelibrary.com]
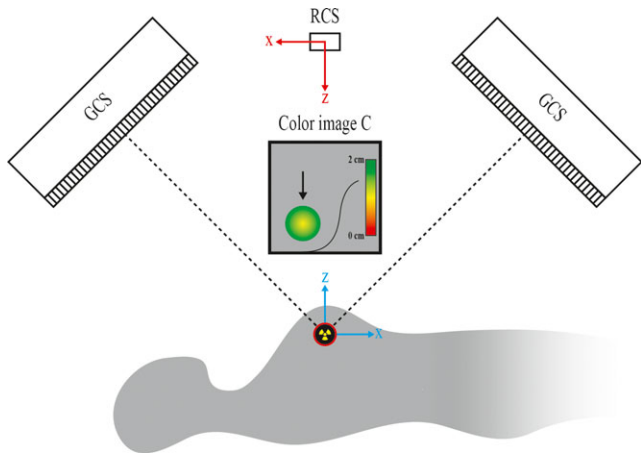
FIG. 2. The INCISE system. The target volume to be visualized is depicted in red and black (positioned within the patient). An overlay of a video image from the range-camera system (RCS) and the target volume is indicated with the black arrow. The location of the seed is indicated by the yellow radiation symbol within the target volume. The coordinate systems of the RCS and the gamma-camera system (GCS) are depicted in red (upper one) and blue (lower one), respectively. [Color figure can be viewed at wileyonlinelibrary.com]

2.A.2. Triangulation of seed location from biplanar views

A procedure was developed to reconstruct 3D RS locations from two biplanar views of the GCS. The first purpose of this procedure is to triangulate the 3D RS location in the tumor (Fig. 3, as described in detail in Ref. [15]). The second is to establish the 3D RS locations in the calibration phantom that contains multiple iodine-125 seeds. This is required for our calibration procedure, which is described in detail in Section 2.A.4.

A Gaussian mixture model and an expectation–maximization algorithm were used to allow localization of several 2D RS locations simultaneously in one projection view. As described in Appendix A, these algorithms were modified to make them more robust to scattered counts and background
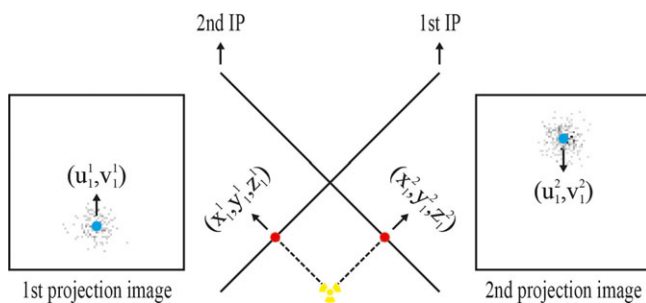

FIG. 3. Triangulation of a radioactive seed (RS) from biplanar views. To visualize the target volume, the 3D RS location was triangulated. The same procedure was used to establish the 3D RS locations in the calibration phantom that contains multiple iodine-125 seeds. The RS locations in the projection views are depicted in blue. Their corresponding 3D locations on the image planes are depicted in red. The actual 3D RS location is indicated by the yellow radiation symbol. [Color figure can be viewed at wileyonlinelibrary.com]

counts. As indicated in Fig. 3, all 2D RS locations in the projection views were transformed to the corresponding 3D locations on the corresponding image planes (IPs):

$$\left(x_k^1, y_k^1, z_k^1\right)^T = R_{01}\left(u_k^1, v_k^1, 0\right)^T \tag{1}$$

$$\left(x_k^2, y_k^2, z_k^2\right)^T = R_{02}\left(u_k^2, v_k^2, 0\right)^T \tag{2}$$

where $\{k \in \mathbb{N}, 1 \leq k \leq 4\}$, $\left(u_k^1, v_k^1\right)$ denotes the kth 2D RS location estimated from the first GCS-detected projection image, $\left(u_k^2, v_k^2\right)$ denotes the kth 2D RS location estimated from the second GCS-detected projection image, R_{01} denotes the first image-to-world coordinate system transformation, and R_{02} denotes the second image-to-world coordinate system transformation. A well-known method for triangulation that finds a midpoint of a common perpendicular was used to establish the actual 3D RS locations from the corresponding 3D IP locations.[11]

2.A.3. The range-camera system (RCS)

We used an SR4500 (MESA Imaging) range camera, which has dimensions of $119 \times 75 \times 69$ mm, detection range from 0 to 9 m, and frame rates from 10 to 30 frames per second. The SR4500 records two images per acquisition: one video image I and one range image. To record the range image, this system generates and at the same time detects a modulated infrared signal that covers the entire breast. Based on the time delay (i.e., phase difference) between the generated signal and the detected signal, SR4500 calculates the distance to the surface of the breast. Comprehensive description related to this measurement approach is outside the scope of this paper, but can be found in Ref. [12]. The camera transforms each range image into a set of surface images, denoted by X_R, Y_R, and Z_R. They contain surface points along the x-axis, y-axis, and z-axis (i.e., vertical axis) of the RCS, respectively. The transformation of X_R, Y_R, and Z_R to surface images X_G, Y_G, and Z_G that contain surface points within the coordinate system of the GCS is described in Section 2.A.4.

2.A.4. Registration between range-camera system and gamma-camera system

Owing to the unknown positions and orientations of the RCS and the GCS, an empirical approach needs to be used to estimate a rigid transformation that maps surface points in the coordinate systems of the RCS to the corresponding points in the coordinate system of the GCS. A registration phantom was developed for this purpose. This phantom has reference points that can be detected by the GCS and by the RCS (Fig. 4). Iodine-125 seeds (with activity 5.18 MBq) were used to label these points. The details of the approach to estimate the rigid transformation are described below.

The phantom was recorded by each imaging system at 10 different positions along the vertical axis (i.e., z-axis) of the
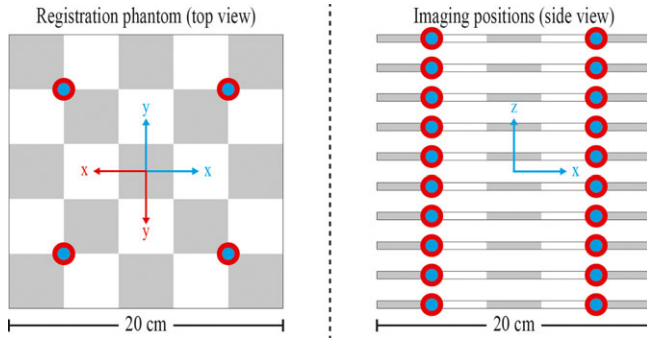
FIG. 4. Registration phantom (left) and 10 imaging positions (right). The coordinate systems of the range-camera system (RCS) and the gamma-camera system (GCS) are depicted in red (lower one) and blue (upper one), respectively. These coordinate systems are also depicted in Fig. 2. Each blue marker denotes the location of one iodine-125 seed. The GCS-detected images were processed to establish these locations. Each red marker denotes the location of one pattern intersection. The RCS-detected images were processed to establish these locations. [Color figure can be viewed at wileyonlinelibrary.com]

GCS. An imaging time of 60 s was used at each position of the phantom to record projection images. These images had a matrix of 128 × 128 and they were used to estimate the 3D RS locations by triangulation, as described in Section 2.A.2. These locations are denoted by $\left(x_G^{ij}, y_G^{ij}, z_G^{ij}\right)$, where i indicates an integer between 1 and 10 that reflects imaging position and j indicates an integer between 1 and 4 that labels the corresponding RS. An integration time of 3.3 ms was used to record one video image and one range image at each position of the phantom. Each RCS-detected image had a matrix of 176 × 144. The 2D RS locations (u_{ij}, v_{ij}) were estimated from the corresponding video images. OpenCV library functions for the detection of chessboard corners were used for this purpose.[13] The RCS-detected locations of the RS in 3D were estimated by:

$$x_R^{ij} = \text{Interp}\left(u_{ij}, v_{ij}, X_R^i\right) \tag{3}$$

$$y_R^{ij} = \text{Interp}\left(u_{ij}, v_{ij}, Y_R^i\right) \tag{4}$$

$$z_R^{ij} = \text{Interp}\left(u_{ij}, v_{ij}, Z_R^i\right) \tag{5}$$

where $\left(x_R^{ij}, y_R^{ij}, z_R^{ij}\right)$ denotes the RCS-detected location of the RS in 3D and $\text{Interp}(u, v, F)$ denotes the linear interpolated value of the surface image F at the location (u, v). In simple words, RCS-detected images were interpolated at the corresponding 2D RS locations to establish the corresponding 3D RS locations. The rigid transformation (i.e., RT) that maps surface points from the coordinate system of the RCS to the coordinate system of the GCS was

estimated from 40 3D RS locations established by the RCS and 40 3D RS locations established by the GCS. The following system of linear equations was solved to estimate this rigid transformation RT:

$$\begin{bmatrix} x_R^{(1)(1)} & y_R^{(1)(1)} & z_R^{(1)(1)} \\ \vdots & \vdots & \vdots \\ x_R^{(1)(4)} & y_R^{(1)(4)} & z_R^{(1)(4)} \\ \vdots & \vdots & \vdots \\ x_R^{(40)(1)} & y_R^{(40)(1)} & z_R^{(40)(1)} \\ \vdots & \vdots & \vdots \\ x_R^{(40)(4)} & y_R^{(40)(4)} & z_R^{(40)(4)} \end{bmatrix} RT$$
$$= \begin{bmatrix} x_G^{(1)(1)} & y_G^{(1)(1)} & z_G^{(1)(1)} \\ \vdots & \vdots & \vdots \\ x_G^{(1)(4)} & y_G^{(1)(4)} & z_G^{(1)(4)} \\ \vdots & \vdots & \vdots \\ x_G^{(40)(1)} & y_G^{(40)(1)} & z_G^{(40)(1)} \\ \vdots & \vdots & \vdots \\ x_G^{(40)(4)} & y_G^{(40)(4)} & z_G^{(40)(4)} \end{bmatrix}$$

Finally, the following expression was used to transform surface points from the coordinate system of the RCS to the coordinate system of the GCS (this is required to estimate distance between the target volume that is defined within the coordinate system of the GCS and the surface of the breast that is detected by the RCS):

$$[X_R(u, v), Y_R(u, v), Z_R(u, v)]RT = [X_G(u, v), Y_G(u, v), Z_G(u, v)] \tag{7}$$

2.A.5. Video overlay

Figure 5 illustrates how a video overlay C is established from a video image I and a distance map D. Here, D reflects the distance between the surface of the breast and the top surface of the target volume along the z-axis of the GCS:

$$D(u, v) = Z_G(u, v) - \max\left(z_G \pm \sqrt{r^2 - (X_G(u, v) - x_G)^2 - (Y_G(u, v) - y_G)^2}\right) \tag{8}$$
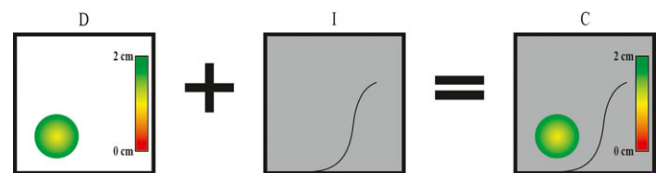

FIG. 5. Visualization of the target volume. A distance map *D* was combined with a video image *I* to produce a video overlay *C* that shows the target volume. A color scale was used for quick distance interpretation. [Color figure can be viewed at wileyonlinelibrary.com]

where (u, v) denotes image coordinates and r denotes the pre-defined radius of the target volume. The part of Eq. (8) within the max function is used in this study to calculate the surface coordinates of the target volume along the z-axis of the GCS (these coordinates are derived from the sphere equation). At locations where the square root is not a real number, no overlay is shown. A look-up-table was used to assign colors to distances, ranging from red (0 cm) to green (more than 2 cm).

2.B. Physical experiments

Physical experiments were conducted to assess the absolute bias and the precision of INCISE. Block phantoms of varying thickness were used (Section 2.B.1), each with one iodine-125 seed with activity of 5.18 MBq. INCISE was used to image these phantoms (Section 2.B.2). The resulting images were processed (Section 2.B.3) to extract the 2D RS locations from which the statistics were generated (Section 2.B.4).

2.B.1. Block phantoms

Each block phantom consisted of a stack of acrylic-based attenuation plates, one of which contained a central pocket with a diameter of 1 mm in which the seed was placed (Fig. 6). The plates have length of 15 cm, width of 12 cm, and thickness of 0.5 cm. Phantom thickness ranged from 3.5 cm to 6.5 cm.

Each phantom was covered with a sheet of white paper. On each sheet, a gray disk was printed with a radius of 2.5 cm. These disks were used for the qualitative assessment of the visualization.

2.B.2. Image acquisition

Figure 7 illustrates the recording setup. The GCS was positioned at a radial distance of 0.4 m. The block phantoms were positioned at a phantom-to-RCS distance of 0.5 m. An imaging time between 1 and 5 s was used to record GCS-detected images (using a matrix of 128×128 pixels). The RCS-detected images were obtained with an integration time of 3.3 ms (using a matrix of 176×144 pixels).

2.B.3. Image processing

RCS-detected and GCS-detected images were processed to extract 2D RS locations. The following system of two nonlinear equations was solved to establish the 2D RS location (u_a, v_a):

$$x = \text{Interp}(u_a, v_a, X_G) \tag{9}$$

$$y = \text{Interp}(u_a, v_a, Y_G) \tag{10}$$

where (x, y, z) denotes the 3D location of the RS. This location, which is depicted in the left part of Fig. 8, represents the measured center of the target volume within the image coordinate system of the RCS. There are two problems that need to be solved to proceed to the next section. First, our 2D RS
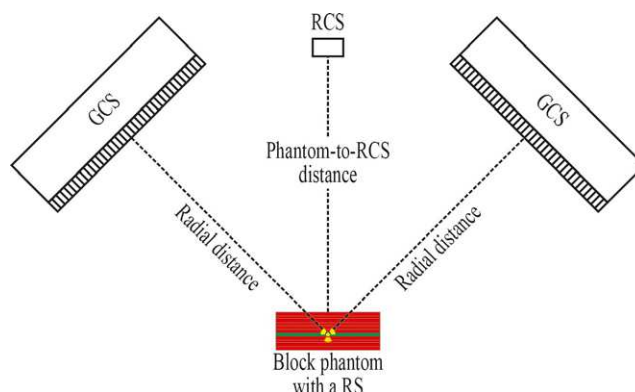

FIG. 7. Image acquisition setup. The range-camera system (RCS) and the gamma-camera system (GCS) were positioned at angles of 90° with respect to the ground plane and 45° with respect to the vertical axis of the RCS, respectively. A radioactive seed (RS) within a block phantom is indicated by the yellow radiation symbol. [Color figure can be viewed at wileyonlinelibrary.com]
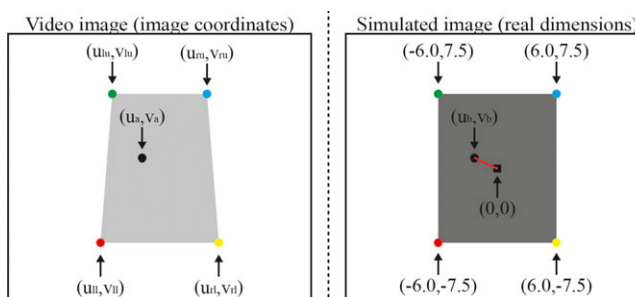

FIG. 8. Video image (left) of the block phantom and the simulated image (right) of the same phantom (both images are illustrations). The corners of the block phantom are depicted with circular markers. Matched corners are depicted with the same color. The 2D locations of the radioactive seed within the simulated coordinate system and the coordinate systems of the range-camera system are denoted by (u_b, v_b) and (u_a, v_a), respectively. Finally, the absolute bias along the horizontal plane is indicated by the red line. [Color figure can be viewed at wileyonlinelibrary.com]
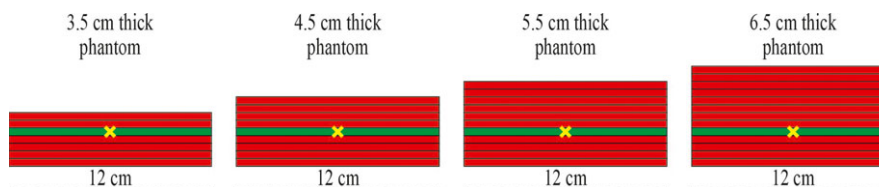

FIG. 6. Each block phantom consists of stacked acrylic-based attenuation plates. One plate (depicted in green) contains a central pocket with an iodine-125 seed (yellow cross). [Color figure can be viewed at wileyonlinelibrary.com]

location is expressed within the image coordinate system of the RCS. Second, image of the block phantom that is associated with this coordinate system is affected by a projective distortion. To solve these problems, we have transformed the 2D RS location to a new 2D RS location (u_b, v_b) within a new coordinate system that contains the simulated image of our block phantom (this location is depicted in the right part of Fig. 8):

$$(u_b, v_b) = TF(u_a, v_a, PT) \tag{11}$$

where $TF(u, v, PT)$ denotes the transformation function that exploits the projective transformation PT to transform the 2D RS location (u, v) from the image coordinate system of the RCS to the coordinate system that contains the simulated image of the block phantom.

The procedure that is described below was used for estimation of PT. First, each corner of the surface of the block phantom was manually denoted within the video image that was detected by the RCS (left part of Fig. 8). These corners were then matched to the corresponding corners of the simulated block phantom (right part of Fig. 8). Finally, PT was estimated from the coordinates of the matched corners.

Figure 8 illustrates that (u_b, v_b) allows us to calculate the absolute bias along the horizontal plane of the proposed system (this bias is indicated by the red line), while (u_a, v_a) does not.

2.B.4. Absolute bias and precision

The vertical distance between the seed and the surface of the block phantom, as determined by the INCISE system, was compared with the known distance d using absolute bias a_a (expressed as mean value) and precision p_a (expressed as standard deviation):

$$a_a = \frac{1}{N} \sum_{k=1}^{N} d_a^k \tag{12}$$

$$(p_a)^2 = \frac{1}{N} \sum_{k=1}^{N} \left(d_a^k - a_a\right)^2 \tag{13}$$

$$d_a^k = \left| d - \left| z_k - Z_G^k\left(u_a^k, v_a^k\right) \right| \right| \tag{14}$$

where N (10) denotes the number of measurements from which a_a and p_a were estimated. The absolute bias a_b and the precision p_b were used to assess the performance with which the target volume was visualized along the horizontal plane of the proposed system:

$$a_b = \frac{1}{N} \sum_{k=1}^{N} d_b^k \tag{15}$$

$$(p_b)^2 = \frac{1}{N} \sum_{k=1}^{N} \left(d_b^k - a_b\right)^2 \tag{16}$$

$$\left(d_b^k\right)^2 = \left(u_b^k\right)^2 + \left(v_b^k\right)^2 \tag{17}$$

3. RESULTS

The absolute bias and the precision along the vertical axis of the INCISE system are given in Table I. The absolute bias was within 4.5 mm for a 6.5 cm thick block phantom, imaged for 5 s at a constant phantom-to-RCS distance of 50 cm.

Along the horizontal plane, the corresponding statistics are given in Table II. The absolute bias was within 2.5 mm for a 6.5 cm thick block phantom imaged for 5 s at phantom-to-RCS distance of 50 cm.

Figure 9 illustrates the output of the video overlay (Section 2.A.5) in the block phantom experiments at 50 cm distance.

4. DISCUSSION

A system for computer-assisted resection of nonpalpable breast lesions (INCISE) was proposed to visualize a "bracketing" sphere centered at the seed in the operating room. This sphere contains the entire tumor (preoperative images are used to define its radius). Physical experiments with block phantoms were performed to assess the absolute bias and the precision of INCISE. These values were 2.1 and 0.8 mm, respectively, along the horizontal plane, and 4.2 and 2.8 mm, respectively, along the vertical axis.

INCISE was designed for use prior to surgery (e.g., to help surgeon to determine the location for the first incision) as well as during surgery. We demonstrated that color-coded

TABLE I. The absolute bias (mm) $\pm$ precision (mm) along the vertical axis of the INCISE system at 50 cm distance between block phantom (BP) and range-camera system.

Seed to BP surface distance (cm)	Imaging time (s)				
	1	2	3	4	5
1.5	3.1 $\pm$ 2.0	3.8 $\pm$ 2.1	3.0 $\pm$ 2.1	2.9 $\pm$ 2.2	3.0 $\pm$ 2.5
2.5	2.9 $\pm$ 2.9	3.7 $\pm$ 2.6	3.2 $\pm$ 2.3	3.5 $\pm$ 2.9	4.0 $\pm$ 3.0
3.5	4.7 $\pm$ 2.7	5.8 $\pm$ 3.3	6.0 $\pm$ 3.5	5.3 $\pm$ 2.7	4.0 $\pm$ 3.2
4.5	5.2 $\pm$ 3.9	4.1 $\pm$ 4.3	3.3 $\pm$ 1.9	3.4 $\pm$ 2.6	4.2 $\pm$ 2.8

TABLE II. The absolute bias (mm) $\pm$ precision (mm) along the horizontal plane of the INCISE system at 50 cm distance between block phantom (BP) and range-camera system.

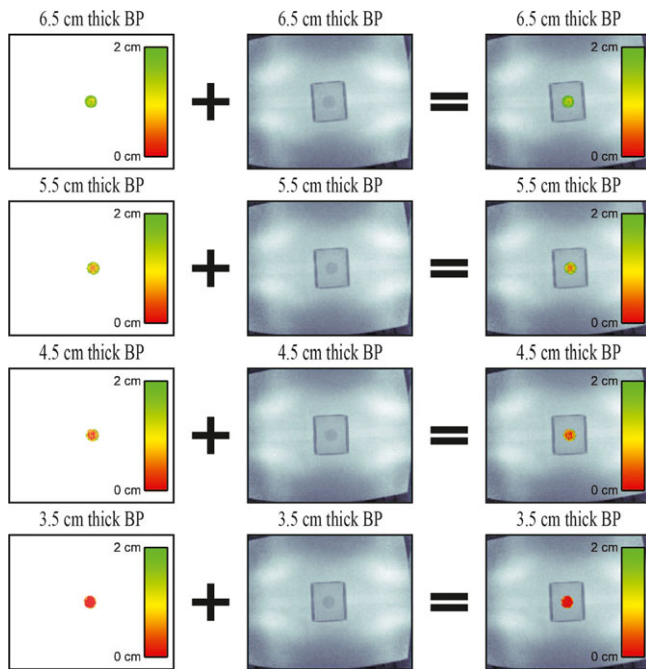| Seed to BP surface distance (cm)	Imaging time (s)				
	1	2	3	4	5
1.5	1.1 $\pm$ 0.5	0.8 $\pm$ 0.4	0.7 $\pm$ 0.4	0.6 $\pm$ 0.4	0.6 $\pm$ 0.3
2.5	3.1 $\pm$ 0.9	2.7 $\pm$ 0.7	2.6 $\pm$ 0.6	2.7 $\pm$ 0.6	1.7 $\pm$ 0.6
3.5	2.4 $\pm$ 1.4	1.5 $\pm$ 0.7	1.4 $\pm$ 0.7	1.0 $\pm$ 0.6	1.8 $\pm$ 0.7
4.5	3.0 $\pm$ 1.5	2.1 $\pm$ 1.1	1.7 $\pm$ 1.1	1.8 $\pm$ 0.9	2.1 $\pm$ 0.8

Fig. 9. Target volume visualization. This volume had a radius of 2.5 cm. Distance map images are illustrated in the first column, video images in the second column, and color images in the third column. [Color figure can be viewed at wileyonlinelibrary.com]

maps of distance between the top surface of the target volume and the surface of the breast can be obtained with a frame-rate of approximately 5 s or less. Thus, intraoperative images can be acquired after the initial incision and the distance overlay can be continuously updated. Accordingly, the RCS is able to track deformations of the surface during surgery.

Park et al.[4] and Singletary et al.[5] demonstrated that local control and cosmetic outcome of BCS can be improved if negative margins are achieved at the primary excision of the tumor. Surgical margins are defined as negative if tumor cells are not present at the cut edge of the excised specimen. For example, Houssami et al. wrote that the minimum margin width for breast cancer types such as ductal carcinoma in situ can vary substantially from 1 to 10 mm and sometimes even more.[14] In the present study, we have demonstrated that the target volume can be visualized with an absolute bias of 5 mm or less. These results are promising because surgical safety margins can be larger than 5 mm.

Our results indicate that the absolute bias and the precision along the horizontal plane are superior to those along the vertical axis. The geometry-dependent attenuation of the signal from the RS, as described in Ref. [15], within each block phantom is probably the main cause of this anisotropy. In short, the geometry-depended attenuation is smaller for the photons that are detected closer to the vertical axis of the GCS than for those that are detected further off-axis (these photons travel along the lines between the seed and the RCS-detected surface of the BP). This difference in the attenuation increased the asymmetry of the observed image-count distributions, which in turn were used to estimate the 3D RS

locations. It is likely that the symmetry of these distributions will be increased if anthropomorphic breast phantoms are used. These phantoms were, however, not used in the present study to enable quantitative and reproducible assessment of the absolute bias and the precision.

The GCS was a clinical single photon emission computed tomography (SPECT) system. A radial distance of 0.4 m was used to record the signal from the seed. This is the maximum distance allowed by the SPECT system. The impact of different collimator-source distances on the localization absolute bias of INCISE was recently investigated.[10] Absolute biases of 3.4 and 3.7 mm were observed for collimator-source distances of 0.5 and 1 m, respectively. These results were obtained with a 6.5 cm thick block phantom recorded for 5 s. Consequently, we hypothesize that the absolute bias with which the target volume can be visualized will not change much if the GCS is positioned at a radial distance larger than 0.4 m. Furthermore, this study also addressed problems such as inherent deficiencies of the GCS (e.g., imaging noise), low-energy photon attenuation, and scatter in the breast, partial volume effect of the small RS. The results from the study show that the combined influence of these drawbacks is not large enough to hamper the application of the GCS. This was additionally confirmed by Ref. [15], where it is demonstrated that collimators with high resolution at large distance cannot be used to significantly improve the performance of the GCS due to the tradeoff between their resolution and sensitivity.

The MESA time-of-flight camera has several limitations that may cause systematic deviations in their output distance maps.[16] Calibration methods were developed to compensate for the influence of some of these errors.[17,18] One approach is to average the distance information over time. Like Linder et al., we suggest averaging raw images over time rather than averaging estimated distance information.[19] To reduce nonlinear deviations, nonrigid transformations may be employed to map surface points from the coordinate system of the RCS to that of the GCS. These methods are subject of future research.

The freehand SPECT system in Ref. [20] is designed to visualize tomographic images in relation to the patient. To the best of our knowledge, there are only two studies in which this system was used for BCS.[21,22] Bluemel et al. reported positive margins in 19% of patients with tumors that were marked with deposits of technetium-99m-nanocolloid. Pouw et al. used freehand SPECT to localize lesions that were marked with iodine-125 seeds, but they did not report the percentage of positive margins. The most important advantage of freehand SPECT is that it visualizes tomographic images in relation to the patient in the operating room. The most important disadvantage is that it takes between 1 and 3 min to record these images.[23–25]

An alternative approach to the GCS described here, is to use a nonradiographic marker that can be localized, for instance, by an x-ray system. A disadvantage is, however, that real-time tracking of the marker under continuous x-ray imaging would increase the dose to the patient. Moreover, while RSL is a standard of care in many breast cancer clinics,

stereotactic x-ray imaging during breast cancer surgery would imply a major change in existing workflow. Another alternative is to use isotopes as markers that emit photons with higher energy than iodine-125. For example, technetium-99m emits photons with energy of 140 keV. This isotope has, however, a half-life of approximately 6 h, which is 238 times shorter than that of iodine-125. Consequently, technetium-99m cannot be injected several days before surgery, which is not the case with iodine-125 seeds. Moreover, seeds containing other isotopes than iodine-125 are not readily available, and would require changes in clinical workflow as well as changes in safety protocols.

Near-infrared agents such as methylene blue and indocyanine green have been used in combination with near-infrared imaging systems such as Mini-FLARE to visualize tumors during BCS. Tummers et al. reported that up to 83% of breast lesions were detected by Mini-FLARE after BCS (these lesions were stained with methylene blue).[26] Near-infrared agents such as indocyanine green were found to allow detection at depths up to 21 mm from the surface of the breast.[27] Consequently, alternative methods such as those that exploit iodine-125 seeds need to be used to localize lesion that are further away from the surface of the breast.

This study has two novelties. First, INCISE is the first system to visualize a bracketing sphere around the seed by taking extent of the tumor into account from the same diagnostic images that are used to plan the surgery. Second, a new method to register a GCS and a RCS was presented.

Planning of breast-conserving surgery is a multidisciplinary effort, involving not only surgeons but also radiologists (for interpretation of images) and pathologists (for interpretation of biopsies and disease spread). Prior to surgery, consensus has already been reached between these disciplines about which areas should be considered cancer and removed. If the region exceeds 3 cm in diameter, BCS may not even be possible. Decades of imaging-pathology studies around mammography, ultrasound, and MRI have provided well-documented information of the accuracy to depict tumor extent.[28,29] Nonetheless, other studies have shown poor correlation between the size of the excision specimen and the size of the tumor, as well as typical asymmetric placement of the tumor in the excision specimens.[30,31] Hence, even if tumor extent has been properly defined beforehand, symmetric excision of this region remains challenging, sometimes causing too much breast tissue to be removed on one side, while safety margins are compromised on the other side. INCISE aims to transfer the consensus on areas that need to be removed directly to the operating theater. This approach has, however, also some disadvantages. First, the tumor may have an irregular shape while the target volume is always spherical. Under these conditions, more tissue may be excised than required. However, asymmetric excisions without guidance also cause surplus of normal tissue to be removed. Because cancers in BCS are typically small (less than 3 cm in diameter), it remains to be investigated whether irregularity of such tumors will lead to larger or perhaps even smaller excision

volumes than currently achieved. Second, the tumor may deform during surgery. The radius of the target volume should take such uncertainty into consideration. Because diagnostic breast images already contain clues about the deformability of the tumor (mammography is performed under heavy compression, ultrasound under variable compression and MRI without compression), future work could focus on biomechanical models to adjust the radius of the spherical target when required. However, we would like to point out that this problem exists in clinical practice independently of INCISE. Third, the diagnostic images may not always accurately reflect the extent of the tumor. This is a problem that transcends INCISE. It also exists in current clinical practice. It is, however, well documented which subgroups of tumors are associated most likely with this issue, e.g., lobular cancers.

This study has several limitations. First, we were unable to test INCISE under conditions that closely mimic those in the operating theater. A clinical dual-head SPECT system was used to estimate the absolute bias and the precision. Ultimately, portable gamma-camera heads may be used to ensure that the surgeon has free access to the patient. Because portable gamma cameras have similar intrinsic resolution as clinical gamma cameras, the results are expected to be comparable. The second limitation is that the block phantoms do not mimic typical clinical situations. For example, they do not mimic breathing that can have an impact on INCISE. This is, however, not expected to have considerable effect, because patients under general anesthesia typically have shallow breathing pattern. On the other hand, home-made phantoms such as anthropomorphic phantoms that mimic all clinical situations would render it more difficult to reproduce the results of this study. The third limitation is that INCISE was not investigated under actual clinical conditions. For example, it was assumed that the RS is positioned close to the center of the tumor. If not, the corresponding target volume will need to be made larger to account for this displacement. Although these first experiments show promising feasibility of the approach, further investigation in patients is required.

5. CONCLUSIONS

A system for computer-assisted resection of nonpalpable breast lesions (INCISE) was proposed to visualize a target volume centered on the location of an iodine-125 seed. Physical experiments with block phantoms were conducted to assess the absolute bias and the precision with which this volume can be visualized. Our results show that INCISE is technically feasible. A follow-up clinical study should be conducted to assess the clinical feasibility.

ACKNOWLEDGMENTS

the EU research program ITEA (Information Technology for European Advancement); project ITEA 09039.

CONFLICTS OF INTEREST

The authors have no relevant conflicts of interest to disclose.

APPENDIX A

A method that was used to extract one or more 2D RS locations from each projection image is described in this appendix. To account for background counts, we assumed that image counts $x_i = (u_i, v_i)$ arranged in a vector $X = \{x_1, x_2, \ldots, x_N\}$ arise from a random vector with the following probability density function:

$$P(x_i|\Theta) = \pi_0 c + \sum_{k=1}^{K} \pi_k p_k(x_i|\mu_k, \Sigma_k) \tag{18}$$

$$\Theta = \{\theta_1, \theta_2, \ldots, \theta_K\} \tag{19}$$

where $p_k(x_i|\mu_k, \Sigma_k)$ is the 2D Gaussian mixture component, $\theta_k = (\pi_k, \mu_k, \Sigma_k)$ is the mixture parameter vector, π_k is the mixture proportion, μ_k is the mixture mean, Σ_k is the mixture covariance matrix, K is the number of mixture components (i.e., the number of iodine-125 seeds), and c is the background suppression constant. This constant had an empirically determined value of 6.1E-5. The expectation–maximization (EM) algorithm was modified to find the estimates of the probability density function parameters. During the first step, we found a probability p_{ik} that image count x_i belongs to the 2D Gaussian mixture component $p_k(x_i|\mu_k, \Sigma_k)$ and probability p_{i0} that image count x_i belongs to the background:

$$p_{ik} = \frac{\pi_k p_k(x_i|\mu_k, \Sigma_k)}{\pi_0 + \sum_{j=1}^{K} \pi_j p_j(x_i|\mu_j, \Sigma_j)} \tag{20}$$

$$p_{i0} = \frac{C}{\pi_0 + \sum_{j=1}^{K} \pi_j p_j(x_i|\mu_j, \Sigma_j)} \tag{21}$$

During the second step, we found the estimates of the probability density function parameters:

$$\pi_k = \frac{1}{N} \sum_{i=1}^{N} p_{ik} \tag{22}$$

$$\pi_0 = 1 - \sum_{k=1}^{K} \pi_k \tag{23}$$

$$\mu_k = \frac{\sum_{i=1}^{N} p_{ik} x_i}{\sum_{i=1}^{N} p_{ik}} \tag{24}$$

$$\Sigma_k = \frac{\sum_{i=1}^{N} p_{ik}(x_i - \mu_k)(x_i - \mu_k)^T}{\sum_{i=1}^{N} p_{ik}} \tag{25}$$

These two steps of the modified EM algorithm were repeated 100 times to estimate one or more 2D RS locations (i.e., μ_k was used in this study as the kth 2D RS location).

[a] Author to whom correspondence should be addressed. Electronic mail: k.g.a.gilhuijs@umcutrecht.nl.

REFERENCES

1. National Comprehensive Cancer Network (NCCN): Breast Cancer. Available from: https://www.nccn.org/professionals/physician_gls/pdf/breast.pdf. Accessed October 27, 2017.
2. van Dongen JA, Voogd AC, Fentiman IS, Legrand C, Sylvester RJ, Tong D, et al. Long-term results of a randomized trial comparing breast-conserving therapy with mastectomy: European Organization for Research and Treatment of Cancer 10801 trial. *J Natl Cancer Inst*. 2000;92:1143–1150.
3. Veronesi U, Cascinelli N, Mariani L, Greco M, Saccozzi R, Luini A, et al. Twenty-year follow-up of a randomized study comparing breast-conserving surgery with radical mastectomy for early breast cancer. *N Engl J Med*. 2002;347:1227–1232.
4. Park CC, Mitsumori M, Nixon A, Recht A, Connolly J, Gelman R, et al. Outcome at 8 years after breast-conserving surgery and radiation therapy for invasive breast cancer: influence of margin status and systemic therapy on local recurrence. *J Clin Oncol*. 2000;18:1668–1675.
5. Singletary SE. Surgical margins in patients with early-stage breast cancer treated with breast conservation therapy. *Am J Surg*. 2002;184:383–393.
6. Nadeem R, Chagla LS, Harris O, Desmond S, Thind R, Titterrell C, et al. Occult breast lesions: a comparison between radioguided occult lesion localisation (ROLL) vs. wire-guided lumpectomy (WGL). *Breast*. 2005;14:283–289.
7. Medina-Franco H, Abarca-Perez L, Garcia-Alvarez MN, Ulloa-Gomez JL, Romero-Trejo C, Sepulveda-Mendez J. Radioguided occult lesion localization (ROLL) versus wire-guided lumpectomy for non-palpable breast lesions: a randomized prospective evaluation. *J Surg Oncol*. 2008;97:108–111.
8. Sakakibara M, Nagashima T, Sangai T, Nakamura R, Fujimoto H, Arai M, et al. Breast-conserving surgery using projection and reproduction techniques of surgical-position breast MRI in patients with ductal carcinoma in situ of the breast. *J Am Coll Surg*. 2008;207:62–68.
9. Nakamura R, Nagashima T, Sakakibara M, Sangai T, Fujimoto H, Arai M, et al. Breast-conserving surgery using supine magnetic resonance imaging in breast cancer patients receiving neoadjuvant chemotherapy. *Breast*. 2008;17:245–251.
10. Arsenali B, de Jong HW, Viergever MA, Dickerscheid DB, Beijst C, Gilhuijs KG. Dual-head gamma camera system for intraoperative localization of radioactive seeds. *Phys Med Biol*. 2015;60:7655–7670.
11. Hartley RI, Sturm P. Triangulation. *Comput Vis Image Und*. 1997;68:146–157.
12. Lange R, Seitz P. Solid-state time-of-flight range camera. *IEEE J Quantum Electron*. 2001;37:390–397.
13. Bradski G, Kaehler A. *Learning OpenCV: Computer Vision with the OpenCV Library*. Sebastopol, CA: O'Reilly Media; 2008.
14. Houssami N, Marinovich ML. Margins in breast-conserving surgery for early breast cancer: how much is good enough? *Curr Breast Cancer Rep*. 2016;8:1–8.
15. Arsenali B, Gilhuijs KG, Viergever MA, de Jong HW. Optimization of parallel-hole collimators for intraoperative localization of iodine-125 seeds. *IEEE Trans Nucl Sci*. 2016;63:2527–2532.
16. Foix S, Alenya G, Torras C. Lock-in time-of-flight (ToF) cameras: a survey. *IEEE Sens J*. 2011;11:1917–1926.
17. Kahlmann T, Ingensand H. Calibration of the fast range imaging camera SwissRanger(TM) for the use in the surveillance of the environment. *P Soc Photo-Opt Ins*. 2006;6396:U7–U18.
18. Lindner M, Kolb A. Lateral and depth calibration of PMD-distance sensors. *Lect Notes Comput Sci*. 2006;4292:524–533.

19. Lindner M, Schiller I, Kolb A, Koch R. Time-of-flight sensor calibration for accurate range sensing. *Comput Vis Image Und*. 2010;114:1318–1328.

20. Wendler T, Herrmann K, Schnelzer A, Lasser T, Traub J, Kutter O, et al. First demonstration of 3-D lymphatic mapping in breast cancer using freehand SPECT. *Eur J Nucl Med Mol Imaging*. 2010;37:1452–1461.

21. Bluemel C, Cramer A, Grossmann C, Kajdi GW, Malzahn U, Lamp N, et al. iROLL: does 3-D radioguided occult lesion localization improve surgical management in early-stage breast cancer? *Eur J Nucl Med Mol Imaging*. 2015;42:1692–1699.

22. Pouw B, de Wit-van der Veen LJ, van Duijnhoven F, Rutgers EJ, Stokkel MP, Valdes Olmos RA, et al. Intraoperative 3D navigation for single or multiple 125I-seed localization in breast-preserving cancer surgery. *Clin Nucl Med*. 2016;41:e216–e220.

23. Bluemel C, Schnelzer A, Okur A, Ehlerding A, Paepke S, Scheidhauer K, et al. Freehand SPECT for image-guided sentinel lymph node biopsy in breast cancer. *Eur J Nucl Med Mol Imaging*. 2013;40:1656–1661.

24. Mihaljevic AL, Rieger A, Belloni B, Hein R, Okur A, Scheidhauer K, et al. Transferring innovative freehand SPECT to the operating room: first experiences with sentinel lymph node biopsy in malignant melanoma. *Eur J Surg Oncol*. 2014;40:42–48.

25. Sulzbacher L, Klinger M, Scheurecker C, Wacha M, Shamiyeh A, Malek M, et al. Clinical usefulness of a novel freehand 3D imaging device for radio-guided intraoperative sentinel lymph node detection in malignant melanoma. *Clin Nucl Med*. 2015;40:e436–e440.

26. Tummers QR, Verbeek FP, Schaafsma BE, Boonstra MC, van der Vorst JR, Liefers GJ, et al. Real-time intraoperative detection of breast cancer using near-infrared fluorescence imaging and Methylene Blue. *Eur J Surg Oncol*. 2014;40:850–858.

27. Pleijhuis RG, Langhout GC, Helfrich W, Themelis G, Sarantopoulos A, Crane LM, et al. Near-infrared fluorescence (NIRF) imaging in breast-conserving surgery: assessing intraoperative techniques in tissue-simulating breast phantoms. *Eur J Surg Oncol*. 2011;37:32–39.

28. Boetes C, Mus RD, Holland R, Barentsz JO, Strijk SP, Wobbes T, et al. Breast tumors: comparative accuracy of MR imaging relative to mammography and US for demonstrating extent. *Radiology*. 1995;197:743–747.

29. Deurloo EE, Klein Zeggelink WF, Teertstra HJ, Peterse JL, Rutgers EJ, Muller SH, et al. Contrast-enhanced MRI in breast cancer patients eligible for breast-conserving therapy: complementary value for subgroups of patients. *Eur Radiol*. 2006;16:692–701.

30. den Hartogh MD, van Asselen B, Monninkhof EM, van den Bosch MA, van Vulpen M, van Diest PJ, et al. Excised and irradiated volumes in relation to the tumor size in breast-conserving therapy. *Breast Cancer Res Treat*. 2011;129:857–865.

31. Stroom J, Schlief A, Alderliesten T, Peterse H, Bartelink H, Gilhuijs K. Using histopathology breast cancer data to reduce clinical target volume margins at radiotherapy. *Int J Radiat Oncol Biol Phys*. 2009;74:898–905.

ClearCheck
One-click plan evaluation
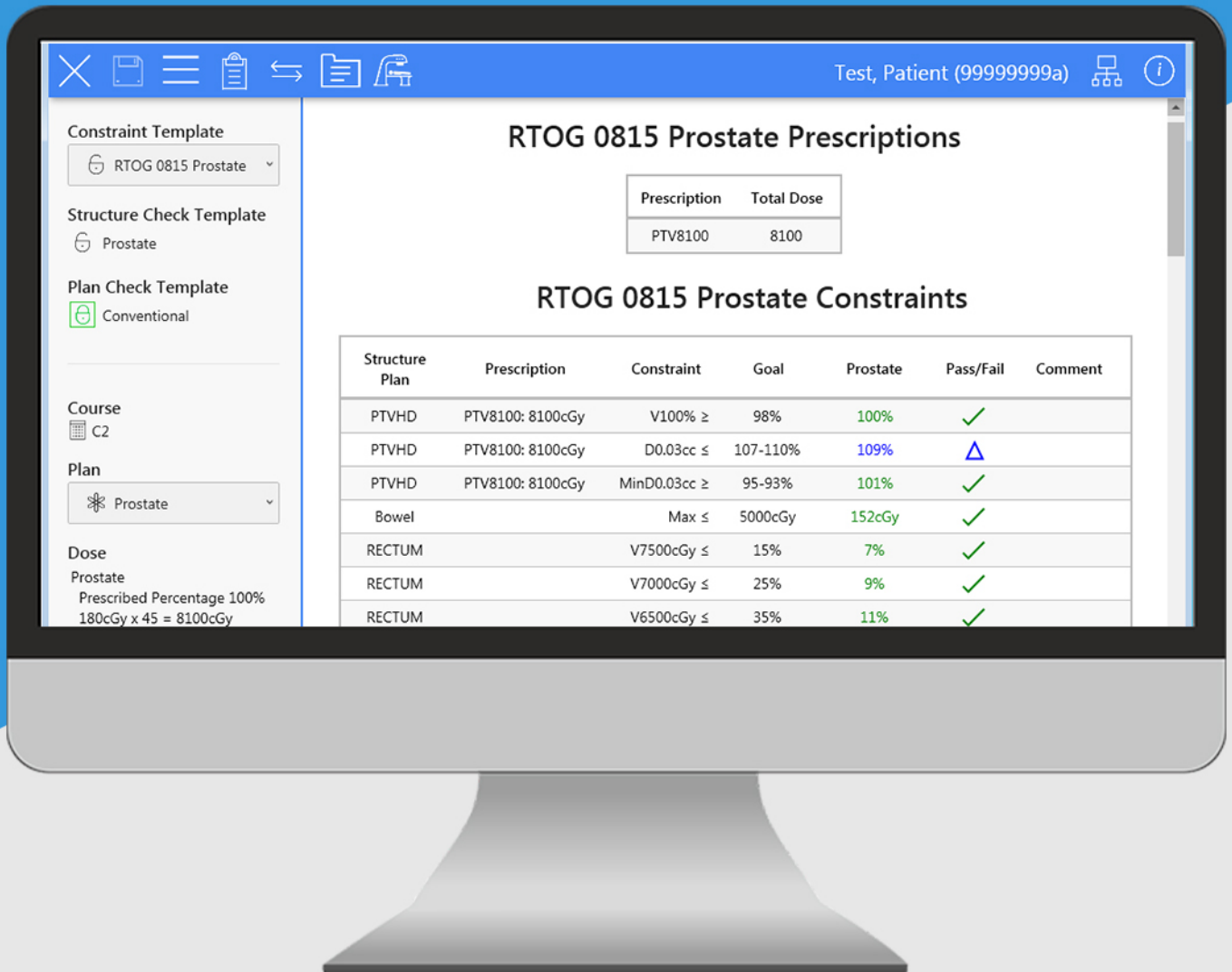
Dose Constraints ◦ Plan Checks
Structure Checks ◦ Collision Checks

RADformation.com